RESEARCH ARTICLE

VOLCANICA

Structural instability within the active crater of Poás volcano, Costa Rica

John Stix*[α], Margaret Kalacska[β], Juan Pablo Arroyo-Mora[γ], Oliver Lucanus[β],
J. Maarten de Moor[δ], Molly Urquhart[α], and Carlos Andrés Campos Vargas[ε]

[α] Department of Earth & Planetary Sciences, McGill University, 3450 University Street, Montreal, Quebec H3A 0E8, Canada.
[β] Applied Remote Sensing Laboratory (ARSL), Department of Geography, McGill University, Montreal, QC H3A 0B9, Canada.
[γ] National Research Council of Canada, Flight Research Laboratory, 1920 Research Road, Ottawa ON K1A 0R6, Canada.
[δ] OVSICORI-UNA, De la UNA 200m N 100m E, Apartado 2386-3000, Heredia 40101, Costa Rica.
[ε] Laboratorio de Investigación e Innovación Tecnológica (LIIT), Universidad Estatal a Distancia (UNED), Montes de Oca, 11503, Costa Rica.

Submitted: 2025-02-22 | Accepted: 2025-07-14 | Published: 2025-10-17

Editor: S. Kanakiya | Typesetter: J. Farquharson

ABSTRACT

This study examines structural patterns in and around the crater of Poás volcano in Costa Rica to determine the current level of stability within the edifice. We used a series of Unoccupied Aerial Vehicle (UAV)-based photogrammetry and thermal infrared surveys to map the active crater, supplemented by satellite imagery to gain a broader view of the regional structural pattern near the volcano. We identified three areas within the eastern crater that exhibit various degrees of instability. The southern sector contains a possible explosion and/or collapse crater; the central zone shows evidence of structural disruption including collapse, fracturing, and/or faulting; and the northern sector contains a new explosion-collapse crater formed in April 2022. Through these three sectors, a principal north–south fault or series of faults truncates the eastern part of the active crater from the rest. These structural patterns continue north and south of the active edifice, demonstrating that east–west extension results in structural weakening at a variety of spatial scales. This weakening is enhanced by rock fracturing caused by volcanotectonic earthquakes and by hydrothermal alteration driven by high-temperature degassing. Because of its instability, the eastern crater area is deserving of further attention from a monitoring and forecasting perspective.

KEYWORDS: Poas volcano; Faulting; Active crater; Instability; Unoccupied aerial vehicle; Photogrammetry; Thermal infrared imaging.

1 INTRODUCTION

Modern volcano monitoring includes seismic, deformation, and gas datasets that are typically collected on a real-time or near-real-time basis. This information affords a detailed assessment of a volcano's current state of unrest, as well as insights into the subsurface plumbing system of the volcano [Pallister and McNutt 2015]. This plumbing can be very complex, including multiple locations where magma is stored [Cashman et al. 2017]. Furthermore, there can be complex interactions between magma and its hydrothermal envelope, which both promote unrest and can lead to eruptions [Stix and de Moor 2018]. These eruptions are typically explosive in nature, with associated hazards for the environment, infrastructure, and people. Understanding and forecasting impending events is always a challenge, because the signals can be subtle, confusing, inconsistent, or contradictory. Poás volcano in Costa Rica is an excellent example of such activity.

Poás is a highly active system with frequent small eruptions, commonly through the summit crater lake. The level of unrest is generally high, and eruptions are typically explosive in nature, either phreatic or phreatomagmatic. Every several decades, more intense explosive magmatic activity occurs at the volcano, with consequent ashfall hazards affecting people, livestock, agriculture and infrastructure. Most recently, a major eruption occurred in April 2017 [Salvage et al. 2018; de Moor et al. 2019], followed by a series of phreatic eruptions in 2019, a small, directed blast and collapse event in the northeastern crater wall in April 2022, a period of phreatic activity in January–April 2024, and intense phreatic and phreatomagmatic activity in the first half of 2025 [OVSICORI 2022; Global Volcanism Program 2024; 2025]. Hence, Poás is a vigorous system requiring constant vigilance and monitoring. These efforts include seismic monitoring, ground deformation studies, and gas observations, including gas fluxes and gas ratios [Salvage et al. 2018; de Moor et al. 2019]. The monitoring at Poás also incorporates data from Unoccupied Aerial Vehicles (UAVs or drones). When integrated, the information gathered generally provides a clear picture of the activity state of the volcano.

Because of its accessibility, Poás has served as a natural laboratory in recent years to develop UAV applications and collect data by UAV. Some examples include sampling water from the crater lake [Sibaja-Brenes et al. 2023], making gas measurements [de Moor et al. 2019], and measuring the isotopic composition of volcanic CO_2 [D'Arcy et al. 2022].

In this paper, we explore new approaches and techniques to understand the volcano and assess its behaviour and activity. We focus on the active crater area, using two different sensors mounted on UAVs to characterize surface conditions within the crater, including a photogrammetric camera and thermal infrared imager. These data are supplemented by WorldView-2 satellite imagery to examine areas beyond the active crater. Our approach is multiscale in nature, including multiple UAV-based instruments, with the crater imaged at various spatial and temporal scales. Our principle objectives are (1) to assess the utility of the datasets collected by UAV, (2) to provide an overview snapshot of surface conditions within the crater at a particular point in time, (3) to analyze the structural geology of the crater area and surrounding region,

---

* stix@eps.mcgill.ca

and (4) to assess and understand the stability and instability conditions of the crater area, and how such conditions might influence or determine future activity at Poás, including hydrothermal alteration, explosive activity, and collapse events.

2 MORPHOLOGY, VOLCANIC ACTIVITY AND STRUCTURAL FRAMEWORK OF POÁS

Poás is a complex stratovolcano located in Alajuela Province in the Cordillera Central of Costa Rica at ~2330–2700 masl (Figure 1–3) [Rouwet et al. 2019]. The summit of Poás is composed of three cones. The youngest and most active, the main crater, measures approximately 773 × 726 m in diameter. The vertical distance from the inner crater rim to the edge of the crater lake is approximately 137 m but varies up to ~40 m depending on the area and depth of the crater lake [Vaselli et al. 2003]. The vertical distance between the Mirador (tourist observational platform) and the crater lake is ~210–250 m. The volcano receives a mean annual precipitation of 2217 mm and has an average daytime temperature of 18 °C with night temperatures decreasing to < 10 °C. The land use surrounding the main crater is predominantly tropical rainforest at higher elevations and a mosaic of agriculture and pasturelands at lower elevations. The crater experiences high wind velocities and rapidly changing cloud over; it is not uncommon to observe a sustained wind speed over 7 $\mathrm{m\,s^{-1}}$ (13.6 kt) and gusts exceeding 17 $\mathrm{m\,s^{-1}}$ (33 kt).

Historically, Poás is Costa Rica's most active volcano. The currently active crater area is dominated by an acid lake and the presence of magma at shallow levels, with the magma supplying the lake with heat and fluids [Rowe et al. 1992]. Beneath the lake is a vigorous hydrothermal system. The intimate interplay among the lake, hydrothermal system, and shallow magma drives unrest and eruptive activity at Poás. Eruptions are principally explosive in nature and generated by the interactions between the magmatic and hydrothermal systems. The bulk of eruptive activity is relatively low-level in nature, with eruptions confined within the active crater. Typical styles of activity include both phreatic and phreatomagmatic events, with persistent fumarolic degassing at the surface and below the lake [de Moor et al. 2016; 2019]. The lake's size and temperature vary significantly over time; if input of heat from below is intense, or if meteoric input is low, then the lake can evaporate, dry up, and disappear before reforming. When this happens, strong degassing is observed from the ground, as well as the presence of pools of molten sulfur [Oppenheimer and Stevenson 1989].

From time to time, larger eruptions occur at Poás. These events have occurred historically in 1834, 1910, 1953–1955, and 2017, with a 48–76-year recurrence interval [Salvage et al. 2018; Mora Amador et al. 2019]. The eruptions have VEI values of 2–3, eruption columns reach several kilometers in height, and small amounts of juvenile magmatic material are expelled, typically in the form of ash, lapilli, scoria, blocks, and bombs. The blocks and bombs can be ejected well beyond the rim of the active crater rim, posing a serious hazard to tourists in the national park. Early stages of such eruptive episodes typically comprise phreatic events that give way to later-stage phreatomagmatic and Strombolian eruptions. The crater lake can evaporate and disappear temporarily during this type of activity [Mora Amador et al. 2019].

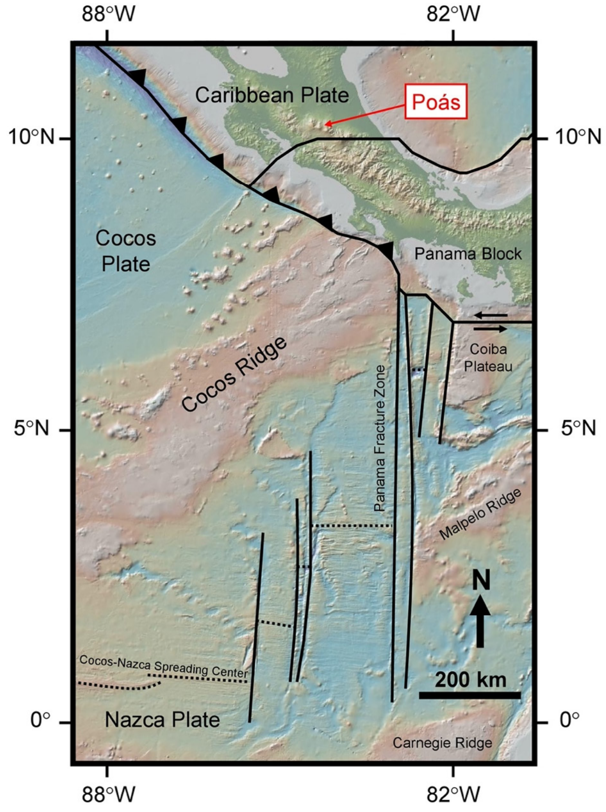

Figure 1: Plate tectonic configuration of the Nicaragua-Costa Rica-Panama portion of the Central America region. Note the north–south fracture zone ~200 km west of the Panama Fracture Zone, which is aligned with Poás volcano to the north. Modified and partly redrawn from Vannucchi and Morgan [2019] using a basemap from `GeoMapApp` version 3.7.4 (http://www.GeoMapApp.org).

From a structural viewpoint, Poás is situated in a complex tectonic environment, both regionally and locally. The Cocos plate is being subducted in a northeast direction beneath Central America at a rate of 7–9 $\mathrm{cm\,yr^{-1}}$ [DeMets 2001] (Figure 1). At 500–1000 km south of the subduction zone, the Cocos and Nazca plates are diverging along the east–west trending Cocos-Nazca spreading center. This divergent zone is offset by several large, north–south trending transform faults, the extension of which intersects the volcano [Vannucchi and Morgan 2019] (Figure 1). This north–south trend is manifested locally by a series of 4–6 monogenetic cones situated 5–10 km south of the active crater, the active crater itself, the Botos and Von Frantzius cones nearby, and Volcán Congo and the Hule and Rio Cuarto maars located 5–14 km to the north of the active crater [Montero et al. 2010] (Figure 4). Hence this north–south alignment may reflect a deep-seated zone of weakness within the crust that could extend downward into the upper mantle. The active crater zone is contained within a series of right-lateral strike-slip faults that trend northwest across

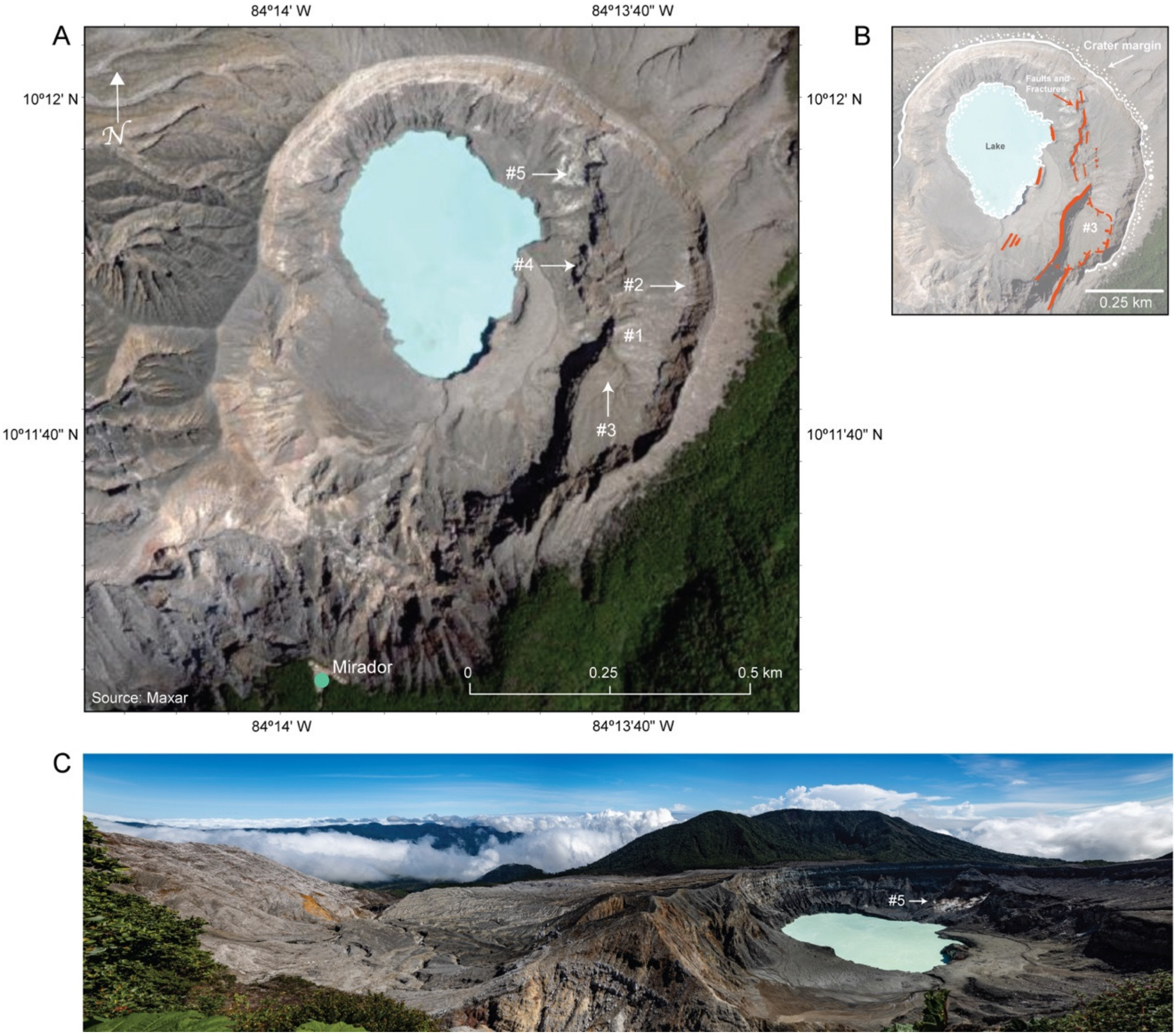

Figure 2: Map of the Poás volcano main crater [A] with drawing [B] illustrating the main geological features of interest. The location of the Mirador (tourist viewpoint) is shown at the south of the image in [A]. The panoramic photograph [C] from the Mirador looking north was taken on 22 June 2022. The numbers correspond to the various features that are discussed in the text. During this time period, the lake water levels were high, and the lake surface area was close to the maximum. The background imagery in [A] is a true colour composite from a WorldView-2 satellite image acquired 26 January 2022, processed as a `Maxar Vivid™` Standard basemap product with 30 cm HD resolution available through the `ArcGIS Pro` World Imagery Basemap product (v.2023.R08).

the area [Montero et al. 2010] (Figure 4), further adding to the structural complexity of the system.

3 METHODS

3.1 UAV photogrammetry

A DJI Matrice 300RTK (hereafter M300) UAV (Da-Jian Innovations, Shenzhen, China) with a DJI P1 photogrammetric camera was used on 22–24 June 2022 to collect RGB photographs of the crater to generate a 3D point cloud and solid mesh digital model (Figure 5). The M300 is an enterprise-grade system, with a 7 kg take-off weight, flight endurance of up to 55 min, 12 $\mathrm{m\,s^{-1}}$ (23 kt) wind resistance, and advanced obstacle detection capabilities. We used a DJI D-RTK 2 Mobile Base Station combined with an Emlid RS2 multi-band GNSS receiver (Emlid Tech Kft, Budapest, Hungary) to determine the precise position of the D-RTK 2 base station through incoming Networked Transport of RTCM (Radio Technical Commission for Maritime Services) via Internet Protocol (NTRIP) corrections from a local commercial GNSS station (operated by PX Receptores GNSS) located within 20 km of the crater. The P1 camera was used with a DJI DL 35 mm F2.8 LS ASPH lens (FOV 84°). The P1 is a full-frame aerial survey camera that acquires 45-megapixel photographs (8192 × 5460 pixels, 4.4 µm pixel pitch) and is integrated directly on the M300 with a 3-axis stabilized gimbal. The pho-

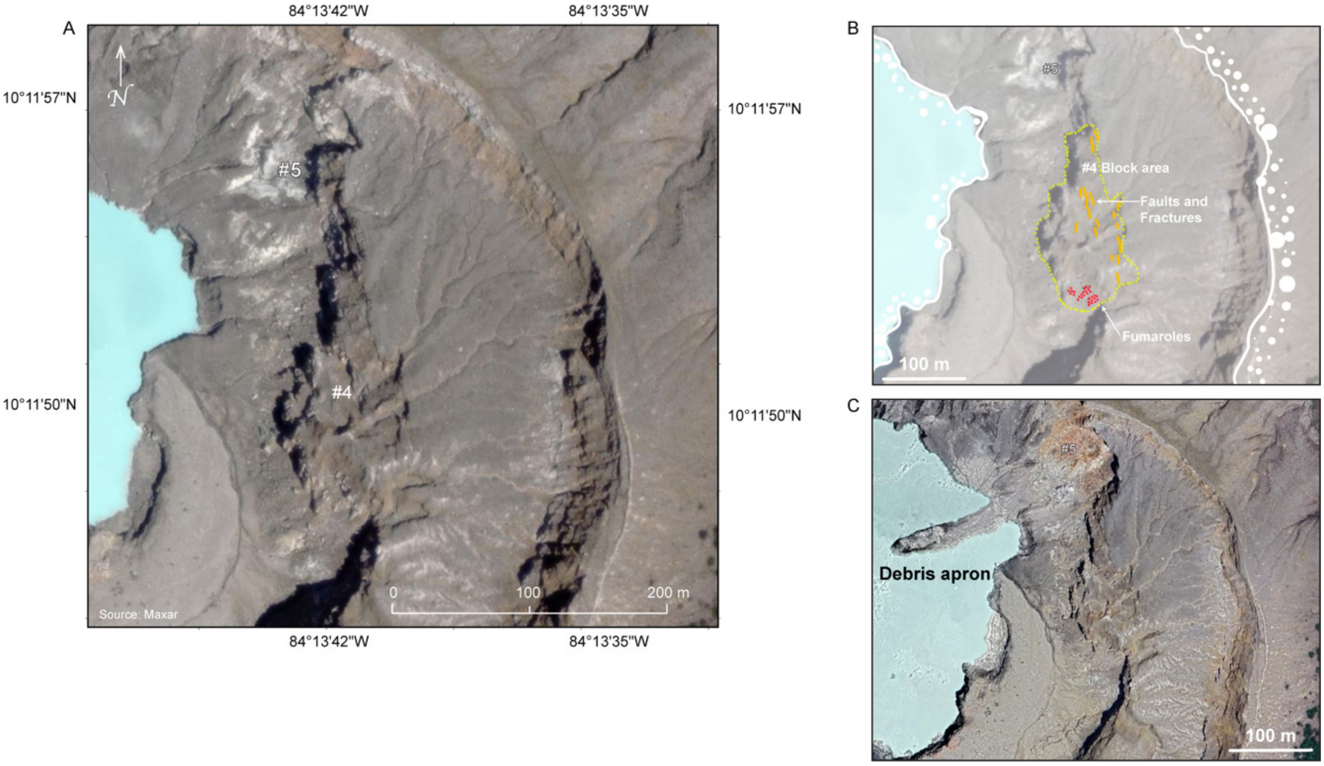

Figure 3: [A] Detail of the eastern crater area. This is a zoomed part of Figure 2A that reveals the structurally complex nature of the block area (Feature #4). The background imagery is the same `Maxar Vivid`™ Standard basemap generated from a WorldView-2 satellite image acquired 26 January 2022, as shown in Figure 2. [B] Image from [A] showing the key characteristics of Feature #4. [C] Screen capture from `Google Earth Pro` illustrating a Pléiades Neo 30 cm resolution image likely acquired 4 May 2023. A debris apron from the 6 April 2022 collapse-explosion event (Feature #5) can be observed extending into the lake on its eastern side. The length of the debris apron is 143 m. The numbers correspond to the various features that are discussed in the text. Orientation is the same in all three panels.

tographs were acquired in both oblique and smart oblique modes at 2634 m HAE (height above ellipsoid) and 2603 m HAE, respectively. In smart oblique mode, the P1 acquires both nadir and oblique photographs. The photographs were collected between 08:20–09:20 in the morning (local time). All UAV flights in this study were conducted in accordance with the permission received from the Costa Rican Civil Aviation Authority and the Poás Volcano National Park.

The photographs were processed using a well-established structure-from-motion (SfM) workflow in `DJI Terra v.3.4.4`. The outputs of interest were an orthomosaic, a 3D point cloud and a solid mesh model [Kalacska et al. 2022]. The total processing times for the orthomosaic and 3D models were 38 min and 101.5 min respectively on a workstation with an Intel Core i7-8086K CPU @ 4.00 GHz, 6.5 GB available RAM and an NVIDIA GeForce GTX 1080 GPU. Measurements of area, volume and linear dimensions of the geological features of interest within the crater were carried out within `Terra`.

3.2 UAV thermal imagery

Thermal infrared (TIR) imagery of the crater was acquired using a DJI Mavic 2 Enterprise Advanced (hereafter M2EA) UAV. The M2EA, with a take-off weight of 0.9 kg, has a dual thermal/visible camera on an integrated 3-axis gimbal, 10 $\mathrm{m\,s^{-1}}$ (19.4 kt) wind speed resistance and 28 min maximum flight time. The thermal camera is sensitive to the 8–14 µm range with a resolution of 640 × 512 pixels and a 46.2° field of view. The Noise Equivalent Differential Temperature (NEDT) is reported as < 50 mK @f1.1 [Leblanc et al. 2021]. The NEDT describes the sensitivity of the camera, which is the root mean square noise of the signal as converted to a temperature difference [Öhman 2014]. UAV flight plans were made in accordance with local weather conditions and topography of the crater, as well as logistics related to take-off from the Mirador. However, during the first night (i.e. "true night" between the end of evening astronomical twilight and the beginning of morning astronomical twilight) acquisition on 21 June 2022, the wind gusts exceeded 8.9 $\mathrm{m\,s^{-1}}$ (17.3 kt) at the farthest point from the take-off location (crater rim on the north side of the lake) and sustained wind speed was > 7 $\mathrm{m\,s^{-1}}$ (13.6 kt) in the W-SW direction, which resulted in the UAV using battery more quickly than anticipated. Due to the difficulties of the UAV's returning 'home' for a battery change, further flights under those conditions were no longer considered safe (conditions exceeding manufacturer's operational limits). Therefore, thermal imaging was accomplished by holding the aircraft over the Mirador railing and pointing the camera towards the thermal area of interest. Imagery was collected this way

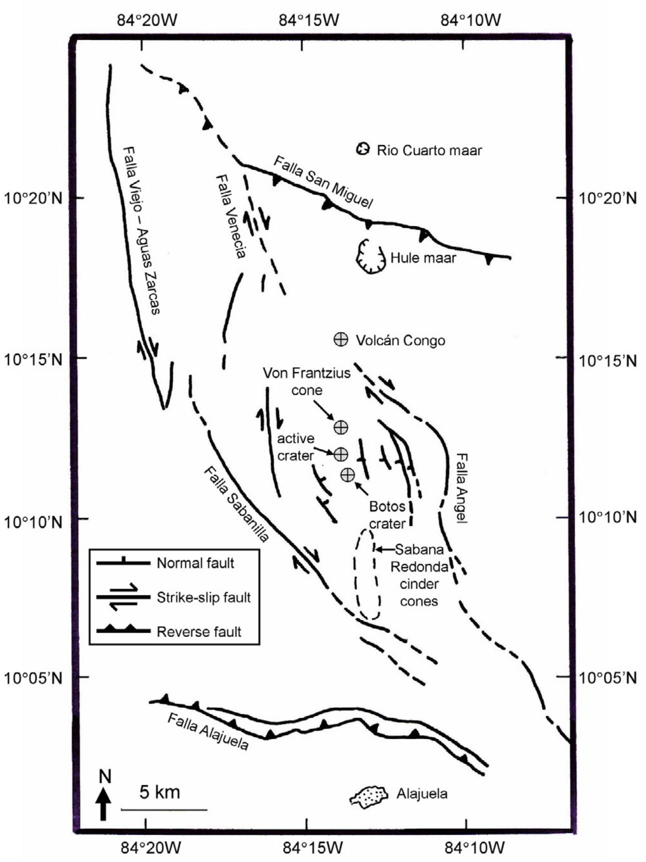

Figure 4: Structural map of the region near Poás, redrawn and modified from Montero et al. [2010].

on 21 June 2022, from 03:21:46–03:24:59 local time, before astronomical twilight starting at 03:57 and sunrise at 05:17 to get a true picture of temperature contrasts across the crater, and to ensure that the temperatures we recorded are due to the volcano itself and not to differences in solar heating.

To estimate ground surface temperature of the crater, the thermal imagery was corrected for emissivity (ε) and environmental factors, including relative humidity and background air temperature [Kuenzer and Dech 2013] using `FLIR Thermal Studio` (Teledyne FLIR, Hudson, NH). Emissivity for the crater materials was determined in the lab according to Section 3.3. For the crater lake, a value of $\varepsilon = 0.98$ from Robinson and Davies [1972] was used.

3.3 Emissivity estimation for crater ground temperature estimation

The emissivities of ash and rock samples that had been collected at eight different locations within the crater in June 2022 were determined experimentally in a laboratory setting. The M2EA was suspended with the thermal camera 1.45 m above the ground, resulting in a pixel size of ~0.19 cm. Each sample was placed on a background of black electrical tape of known emissivity ($\varepsilon = 0.95$) with a second metal plate wrapped in black electrical tape (the industry standard for emissivity calculations) placed next to the samples. The room temperature, barometric pressure and relative humidity were continuously recorded at 1 min intervals with a Sensor Push HTP.xw smart sensor (SensorPush, Brooklyn, NY) that had been previously calibrated for relative humidity using 30 % and 70 % standards. Thermal images of the samples were acquired with this setup in the dark (i.e. room lights were turned off and windows covered with blackout curtains). Using the electrical tape with known ε as reference, the ε for each sample was estimated with `FLIR Thermal Studio` [Vollmer and Möllmann 2010; Mineo and Pappalardo 2021]. The emissivity of each sample from the eight crater locations was averaged (per location). These data were subsequently used to correct for ε in the UAV thermal imagery of the crater as described above in Section 3.2.

3.4 Satellite imagery

The RGB composite from a WorldView-2 satellite image (original 50 cm pixel size) acquired 26 January 2022 and 23 February 2020 and processed as a `Maxar Vivid`™ Standard basemap product with 30 cm HD resolution was available through the `ArcGIS Pro` World Imagery Basemap (v.2023.R08). This imagery has been rendered within the `ArcGIS Pro` imagery basemap product at zoom levels of 12–18. Level 12 is equivalent to a scale of 1:144,448 and level 18 equivalent to a scale of 1:2257. This basemap imagery is used to illustrate regional lineaments and structural trends. While no actual satellite imagery was downloaded and analyzed in this study, we show the potential of various relatively accessible basemaps compiled by other sources for the purpose of large scale visual interpretation.

4 RESULTS

4.1 UAV photogrammetry

Of the 453 photographs that were acquired, 444 were calibrated and used in the generation of the orthomosaic (Figure 6) and 3D models (Figure 7). The nine uncalibrated photographs had excessive steam/gases from the fumaroles obstructing the ground and thus were not used. The final ground sampling distance (GSD) of the orthomosaic was 3 cm (file size of the GeoTIFF = 0.9 GB). The density of the 3D point cloud ranged from 12–98 points m^{-2} with a file size in LAS format of 0.3 GB. The file size of the solid mesh model in I3S format was 1.39 GB. Due to the high-resolution texture of the solid mesh model (up to 8192 × 8192 pixel per block), the structural elements of the crater are reconstructed in very high detail (Figure 7D).

4.2 Volcano crater structure from UAV photogrammetry

The crater itself is sub-circular. In its southern sector, some slumping and mass wasting appear to be occurring. The photogrammetric products (Figure 6 and 7) and satellite imagery (Figure 2 and 3) reveal a crater with a high degree of structural complexity on its eastern side. To the east and southeast of the crater lake is a terraced area that rises to a second higher terrace extending to the eastern crater margin. At the base of this crater margin is a linear, thermally anomalous zone of alteration. The second terrace is identified as Feature #1 on Figure 2, while the thermal zone is shown as Feature #2. From the 3D solid model, this thermal zone is estimated to be 296 m

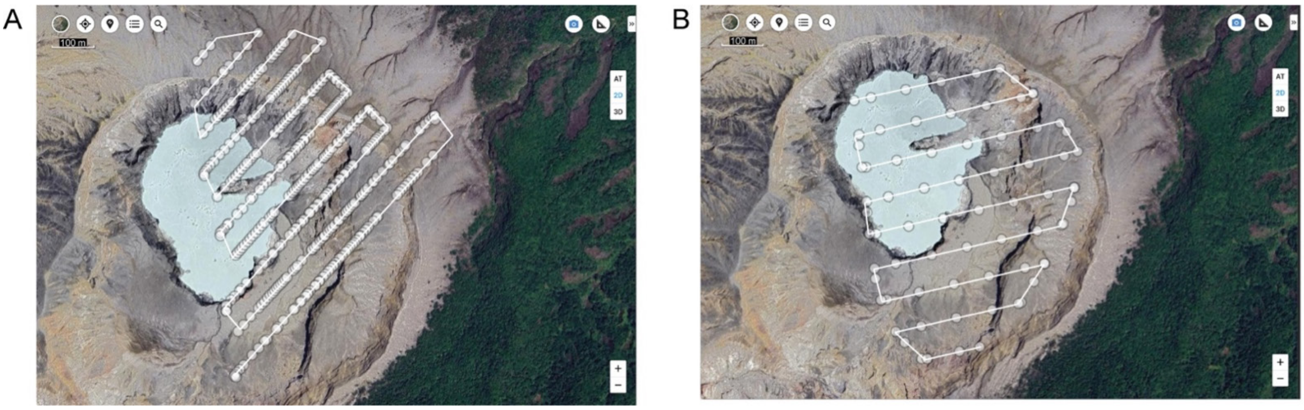

Figure 5: Print screens from DJI Terra illustrating the flight path of the UAV during the photogrammetry data acquisition, as well as the location of the individual photographs (circles) that were taken for [A] smart oblique acquisition and [B] oblique acquisition modes.

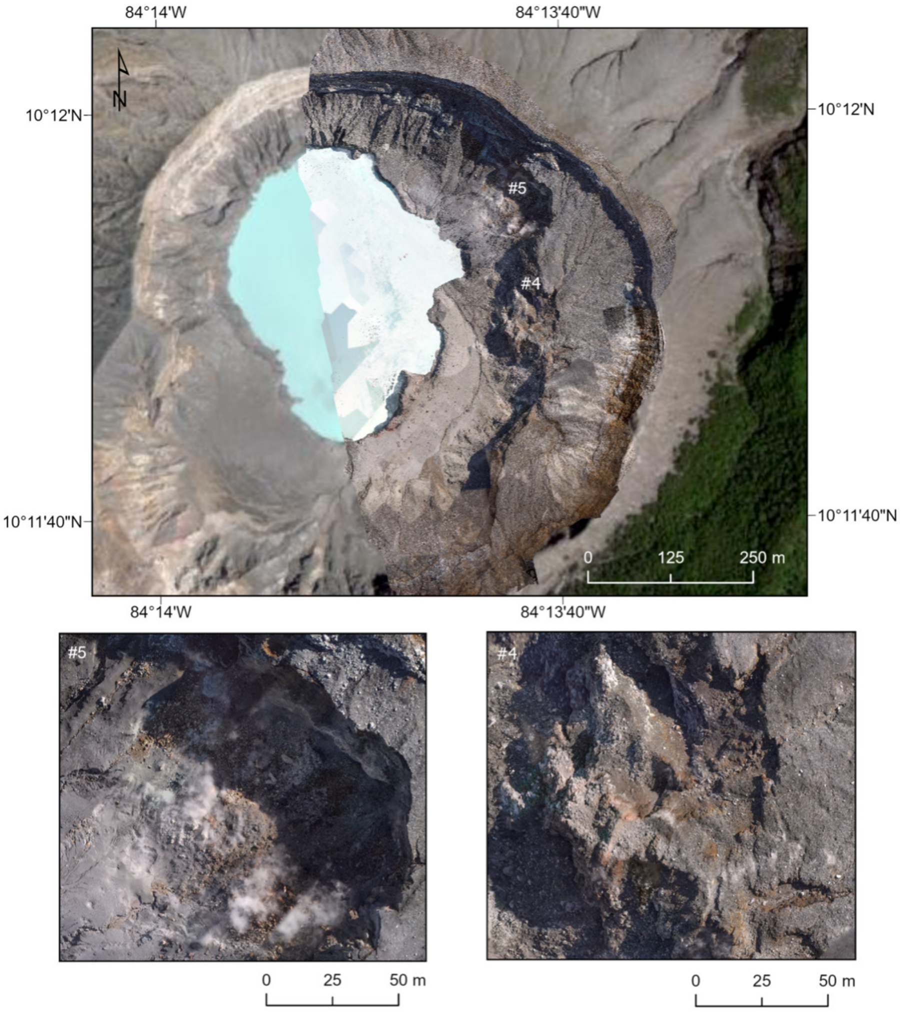

Figure 6: Orthomosaic generated from the UAV photographs at a GSD of 3 cm overlain on the same `Maxar Vivid`™ Standard basemap shown in Figure 2 and Figure 3. The lower map on the right shows a zoomed-in view of Feature #4 (block area), while the lower map on the left shows a zoomed-in view of Feature #5 (collapsed area) from the UAV-generated orthomosaic.

long. The western edge of this higher terrace defines a well-developed structural zone, most likely a fault system, which trends north-northeast and essentially cuts through the entire eastern quarter of the active crater.

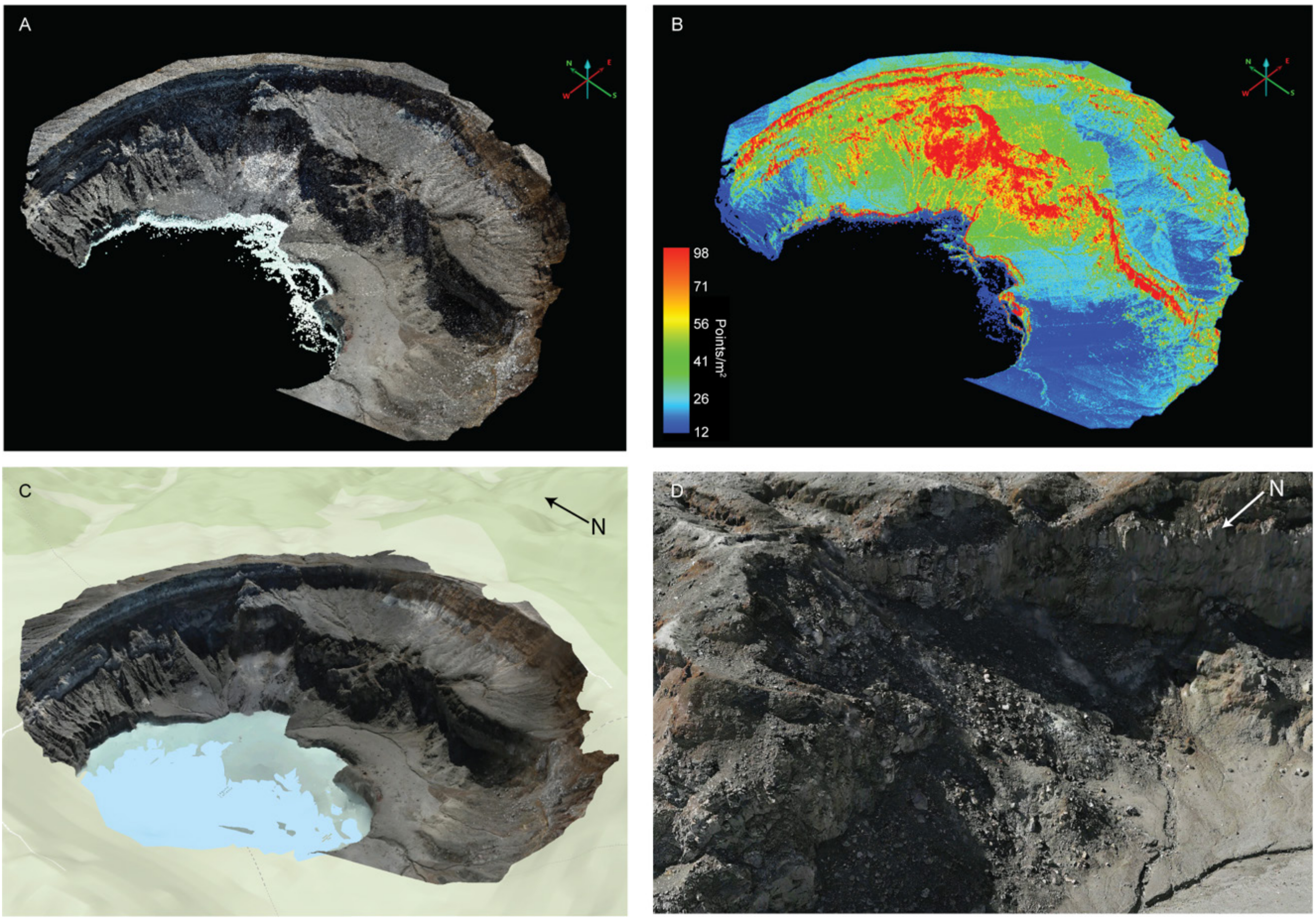

Figure 7: [A] 3D point cloud product from the SfM workflow in Terra. [B] 3D point cloud colourized by point density (points/m^2). [C] Solid mesh model from Terra. Background layer is the ESRI World Elevation3D/Terrain 3D layer with 30 m resolution. [D] Close-up view of 3D detail in the solid mesh model.

This through-going fault zone can be divided into three sectors. The southern sector is defined by a semi-circular area that may be a collapse feature and/or a small crater (Feature #3). To the north is the central sector, a structurally complex block or blocks that may be collapsed, fractured, and/or faulted (Feature #4). This block area is shown in greater detail in Figure 3 and 6, which reveal that faults and fractures at the southern margin are oriented north–south, whereas their orientations moving northward shift slightly to a north-northwesterly trend. Figure 8 is a horizontal view of the solid mesh model of this block area, illustrating the unstable rock masses and talus apron developed adjacent with fumarolic zones near the southern base of the apron. The northern sector comprises the recent collapse and explosion crater formed on 6 April 2022 (Feature #5), displacing about 160,000 m^3 of material [OVSICORI 2022]. The vertical distance between the top rim and the base of this crater is 74 m. At its widest point it is 117 m wide with a fitted area of 12,648.2 m^2. Figure 9A and 9B are vertical and oblique views of the 3D mesh model showing a central degassing zone, white-yellow altered rock exposed in the crater wall, and the remnants of the debris lobes that flowed into the lake during the eruption.

4.3 Thermal imagery

4.3.1 *Emissivity determination*

Experimentally determined emissivity averaged 0.94 (range of 0.916–0.972) across samples collected from within the thermal zone (Feature #2 in Figure 2). The samples consisted predominantly of igneous material such as andesite, felsic tuff, scoria and ash. Samples taken from below Feature #2 (Figure 2) of felsic tuff, basalt, basalt with anhydrite rimming, vesicular and andesitic scoria, and andesite had an average emissivity of 0.94 (range of 0.936–0.948). Background samples of andesite, felsic tuff, vesicular scoria and ash taken from the rim of the crater also had an average emissivity of 0.94 (range of 0.93-0.958). As such, an average $\varepsilon = 0.94$ was used to estimate the surface temperature from the UAV imagery.

4.3.2 *UAV thermal imagery of the crater*

The calculated pixel sizes for the features of interest in the thermal image (Figure 10) are shown in Table 1. The average pixel size for these features is 1.17 m ($\sigma = 0.22$). Following the ε and environmental variable correction, the estimated surface temperatures of the four principal features are shown in Table 2.

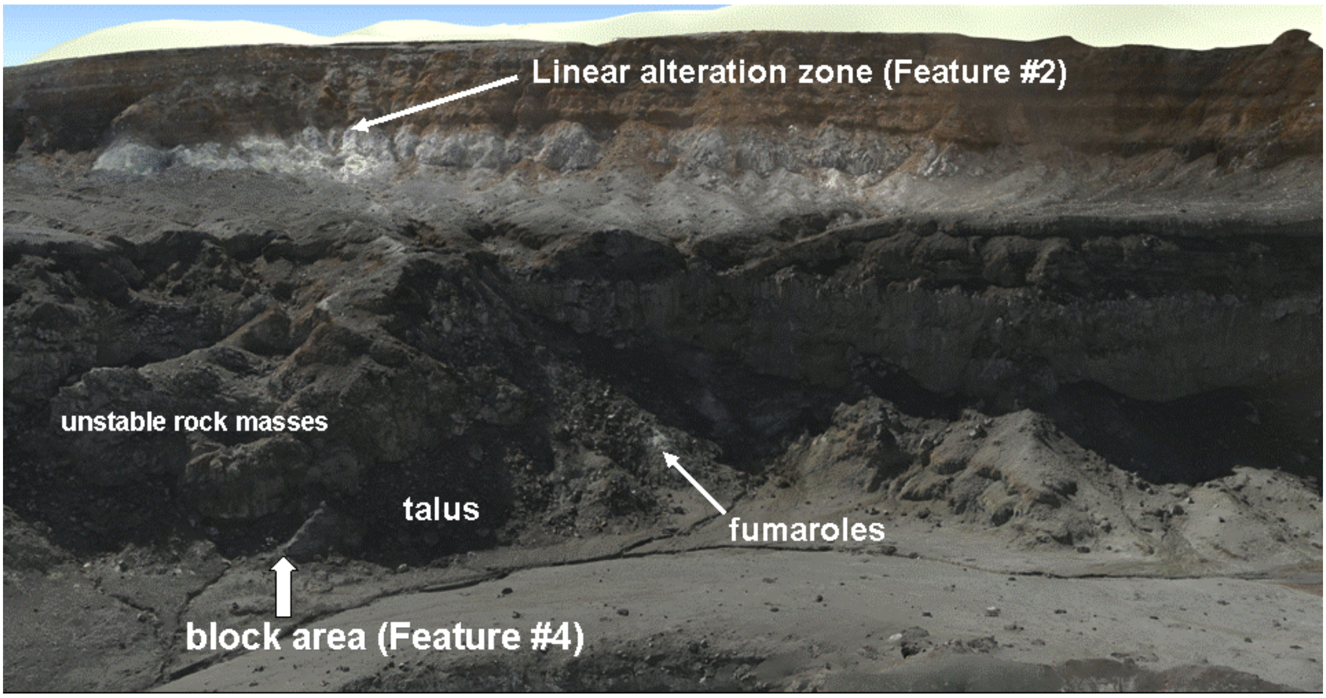

Figure 8: Horizontal view of the 3D solid model showing the structurally complex central area. Unstable rock masses and an adjacent talus apron can be seen, with fumarolic zones near the southern base of the apron.

Table 1: Estimated M2EA thermal image pixel sizes for the various thermal anomalies of interest. Distance is computed to the Mirador from where the imagery was acquired.

Feature	Distance to camera (m)	Estimated pixel size (m)
Near edge of thermal zone (Feature #2)	766.2	1.02
Far edge of thermal zone (Feature #2)	1012.5	1.35
Far edge of lake	1004.9	1.35
Near edge of lake	618.2	0.82
Center of explosion/collapse (Feature #5)	1032.8	1.38
Near edge of block area (Feature #4)	757.4	1.01
Far edge of block area (Feature #4)	957.8	1.28

Table 2: Estimated surface temperature following ε and environmental variable correction for the main thermal features of interest. The values represent the mean and the range (maximum and minimum temperatures).

Feature	Brightness temperature (K)	Celsius equivalent brightness temperature (°C)	Estimated surface temperature (°C)
Crater lake (Feature #1)	303.3 (299.1–306.4)	30.1 (25.9–33.2)	31.2 (26.9 – 34.3)
Linear alteration zone (Feature #2)	294.6 (284.1–310.4)	21.4 (10.9–37.2)	24.4 (13.5 – 40.7)
Explosion/collapse feature (Feature #5)	288.1 (283.7–312.5)	14.9 (10.5–39.3)	17.7 (13.1–42.9)
Fumarolic zone (Feature #4)	286.5 (283.1–303.5)	13.3 (9.9–30.3)	16 (12.5–33.6)
Crater background	282.7 (282.1–283.7)	9.5 (8.9–10.5)	12.1 (11.5–13.2)

The thermal image shown in Figure 10 from which the temperatures in Table 2 were calculated also provides complementary spatial information and shows the location of the four principal features: the crater lake with a maximum temperature of 34.3 °C (Feature #1), the recent collapse/explosion area with maximum temperature 42.9 °C (Feature #5), a fumarolic zone with maximum temperature 33.6 °C that corresponds to the block area discussed above (Feature #4), and the thermally anomalous linear zone of alteration discussed above with maximum temperature 40.7 °C (Feature #2) (Table 2). The four anomalies that are observed correspond well to those seen on thermal infrared images taken immediately after the 6 April 2022 collapse event and explosion [OVSICORI 2022].

On the thermal image (Figure 10), the lake appears to be slightly hotter on its western side (34.3 °C) relative to its east-

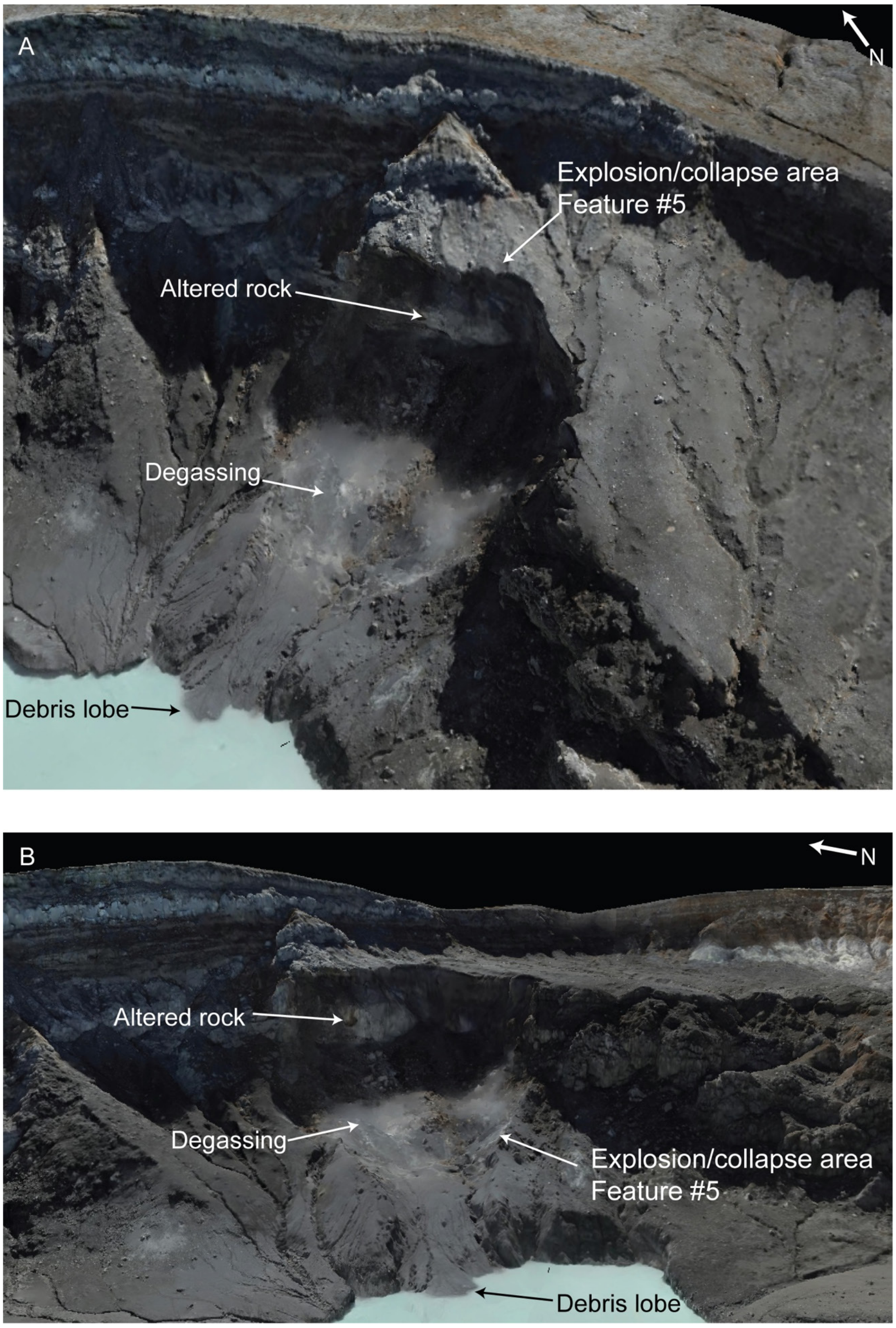

Figure 9: [A] Vertical view of the 3D solid model illustrating the explosion/collapse area generated by the 6 April 2022 eruption crater showing a central degassing zone, exposed white-yellow altered rock exposed in the crater wall, and the remnants of the debris lobes that flowed into the lake during the eruption. [B] Horizontal view of the same area.

ern side (26.9 °C). Apart from the lake, the collapse feature (#5), the zone of alteration (Feature #2) and the block area (Feature #4) show distinct areas of comparatively higher temperatures. The crater outside of these areas has a temperature range < 14 °C. The uppermost part of the block area exhibits a linear feature (Feature #4.1 shown on Figure 10) that may be a fault or fracture. This structure trends north–south and appears to parallel the linear zone of alteration (Feature #2) located ~105 m to the east. The relationship between these two features also can be seen clearly on Figure 3.

4.4 Regional structural patterns

Figure 11 is a satellite image showing regional structural patterns and lineaments beyond the active crater. Several generally north–south trending structures can be seen on this image. A series of parallel faults are observed extending ~5 km to the east and northeast of the crater. Some of these structures have been mapped as normal faults by Montero et al. [2010], and the high fault density seen in this figure indicates significant instability and seismic hazard in this area. At 3.5 km west of the active crater, a well-expressed fault zone is observed that

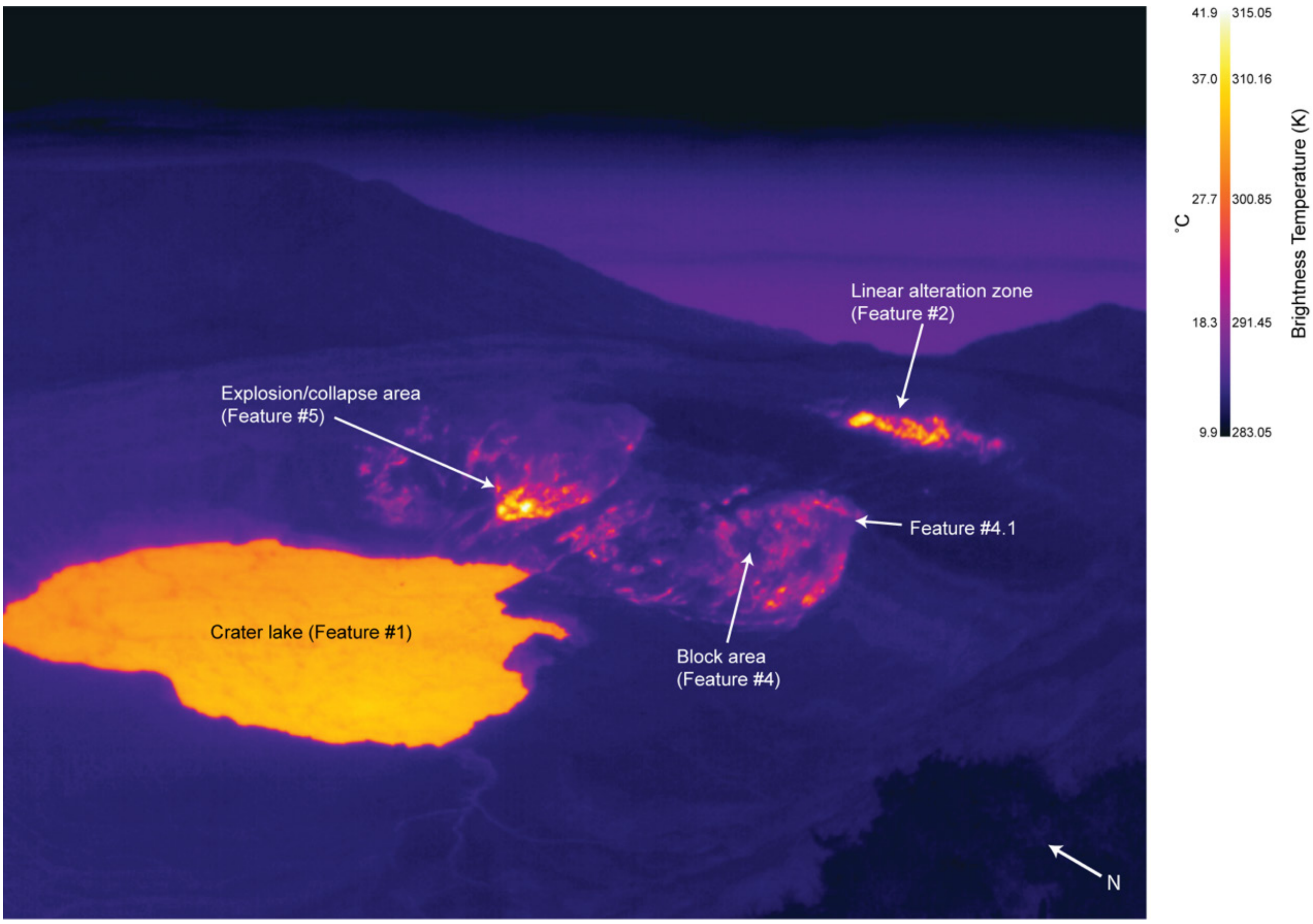

Figure 10: Thermal image of the crater acquired from the Mirador at 03:24:30 local time (09:24:30 UTC) on 21 June 2022. For consistency across the scene the image is shown in brightness temperature with the Celsius equivalent also shown on the colour bar. The numbers correspond to the various features that are discussed in the text.

corresponds to the right-lateral Falla Carbonera mapped by Montero et al. [2010].

5 DISCUSSION

We analyzed several remotely sensed data at various scales to study structural features of both the active crater area and the broader region surrounding the crater. Within the crater itself, we used UAV photogrammetry and thermal infrared data, supplemented by satellite imagery provided through multiple basemap services to examine these features. Further afield beyond the active crater, we used satellite imagery from the `ArcGIS Pro` World Imagery Basemap product to visually interpret and map regional lineaments and structural trends. This imagery product, when integrated, provides a reasonably complete overview of the main features in and around the crater.

Our principal findings are four-fold. First, structural complexity is observed at Poás at various spatial scales, both within and beyond the active crater area. Second, a well-defined fault system in the crater cuts through its eastern quarter. Third, we observe four distinct thermally anomalous zones in the crater. These anomalies correspond well to those seen on thermal infrared images taken immediately after the 6 April 2022 collapse event and explosion [OVSICORI 2022]. Fourth, we observe a highly faulted zone located east and northeast of the crater.

We now integrate our image analysis into four broader themes. First, we examine regional tectonics influencing the volcano. Second, we look at the stability conditions of the active crater area. Third, we address current and future hazards related to structure and tectonics. Fourth, we discuss how various remote sensing platforms can be profitably used and integrated in this type of study.

5.1 Regional tectonics

The well-developed north–south structural trend that we have documented at a range of spatial scales can be placed into a larger volcano-tectonic context. Montero et al. [2010] compiled a variety of structural and seismic data of the region to develop a model of two principal dextral strike-slip faults that trend generally northwest-southeast on either side of Poás (Figure 4). These faults, termed the Falla Sabanilla to the west of the volcano and the Falla Angel to the east, are juxtaposed with two east–west trending reverse fault systems, the Falla Alajuela ~17 km to the south of the volcano and the Falla San Miguel ~14 km to the north (Figure 4).

Figure 11: Satellite image showing regional structural grain and faults beyond the active crater area. The imagery is a true colour composite from a WorldView-2 satellite image acquired 23 February 23 2020, processed as part of the `Maxar Vivid`™ Standard basemap available through the `ArcGIS Pro` World Imagery Basemap product (v.2023.R08).

Between the two strike-slip faults, Montero et al. [2010] mapped a series of arcuate normal faults trending generally north-northwest and forming a series of graben structures within a transtensional structure. Our mapping of structural lineaments, shown in Figure 11, reveals a series of fault structures that have orientations ranging from north-northwest to north-northeast. These are likely related to the mapped normal faults.

Montero et al. [2010] make two additional observations. First, they note that historic earthquakes ranging in magnitude from 5.1 to 6.1 appear to occur on the strike-slip faults. This is significant in terms of ground shaking and stability of the active crater area. Second, they do not see structural evidence for calderas. Brown et al. [1987] and Prosser and Carr [1987] provide evidence for a series of older calderas in the summit region of the volcano. While the arcuate faults mapped by Montero et al. [2010] near the volcano could reflect caldera faults, our structural mapping in this area reveals dominantly linear features (Figure 11). It is possible that the volcanic centers of Botos and Von Frantzius are expressions of the calderas, but the dominant north–south fault system between the two strike-slip structures does not appear to be related to caldera structures.

Montero et al. [2010] propose a model of north–south directed shortening as reflected by the Alajuela and San Miguel reverse faults. Thus, the maximum compressive horizontal force is north–south, with resulting transtensional structures as shown by the two dextral faults within which is an extensional regime dominated by normal faulting and horst-graben structures. Thus, the least compressive horizontal force is east–west, resulting in east–west extension in the region of the volcano.

5.2 North–south volcanotectonic trends and the active crater

The central extensional regime, within which Poás is located, is manifested by the generally north–south trending normal faults and the strong north–south alignment of the various volcanic centers extending nearly 30 km from the Sabana Redonda cinder cones in the south to the Rio Cuarto maar in the north (Figure 4) [Montero et al. 2010]. The active crater of Poás, with the adjacent Botos and Von Frantzius centers, is a central component of this volcanic alignment. Thus we suggest that magmas in this region are transported through the crust by a series of north–south oriented dyke systems that are facilitated by a structurally weak upper crust caused by the east–west extension.

The spatial extent of this north–south oriented tectonic zone is unclear. It may be limited by the Alajuela and San Miguel reverse faults. However, the zone could be considerably larger. Laguna Rio Cuarto, a maar crater, lies to the north of the San Miguel reverse fault and along the same north–south alignment of volcanic features. In a plate tectonic context, a series of north–south transform faults offset the eastern margin of the Cocos-Nazca spreading center [Drummond et al. 1986; Vannucchi and Morgan 2019] (Figure 1). The most prominent of these transform faults is the Panama Fracture Zone. Approximately 200 km west of this fracture zone is another well-expressed series of transform faults, and the projection of these structures northward intersects Poás [Vannucchi and Morgan 2019] (see Figure 1). Hence it is possible that the north–south features observed in the vicinity of Poás are part of a much larger zone of crustal weakness.

The north–south feature is also particularly well displayed at the scale of the active crater. Here a significant through-going structure essentially truncates the entire eastern sector of the crater. The orientation of this structure is north–south with some deviations to the north-northeast and north-northwest. The April 2022 explosion-collapse feature (Feature #5 in Figure 2 and Figure 3 falls on this structure, as does the second possible crater located to the south (Feature #3). Between these two structures lies a zone characterized by small faults and fractures trending north-northwest (Feature #4). Thermal anomalies also trend north–south (see Features #2 and #4.1 in Figure 10). Based on (1) the analysis by Montero et al. [2010] showing east–west extension and (2) the anomalous structural features identified along the eastern crater zone, we conclude that this sector of the volcano is highly unstable, requiring careful monitoring to detect future activity and unrest. The rock masses forming this zone may in fact be slowly collapsing and/or sliding. Such potential movements could be measured on a regular basis to establish rates and detect any accelerations. The simplest way to accomplish this is by photogrammetric and LiDAR surveys by UAV on a regular basis.

5.3 Current and future hazards

Our data and results indicate that the eastern sector of Poás is unstable. This is the result of a number of processes, some of which are ongoing. First, the north–south fault system promotes east–west extension and instability. Second, generally continuous shallow earthquake activity beneath the active crater, in particular high-frequency volcanotectonic events, serve to fracture and break rock, causing weakening. Third, the continual degassing through the crater results in hydrothermal alteration of the rock, further weakening the material. Fourth, the fracturing and alteration can increase rock porosity, which can also reduce rock strength. Fifth, sudden and intense precipitation events, which are very common at the summit of the volcano, result in water infiltration into the shallow subsurface system, loading it temporarily thus promoting instability. Together, these five mechanisms play a significant role in reducing the stability of the eastern crater area.

The shallow magmatic-hydrothermal system beneath the active crater area is likely influenced by the structural complexity and weakness at various scales that are evident on and around the volcano. Magma is probably fed through a system of north–south dykes. This shallow source of heat and gas, as well as structurally permeable roof rocks and wall rocks, promotes a hydrothermal system that can be pressurized at certain times and places, as shown by the April 2022 explosion-collapse event and the possible presence of an older explosion-collapse crater (Feature #3). Pressurization can develop by hydrothermal sealing and/or by injections of new magma accompanied by gas exsolution generating gas bubbles [Stix and de Moor 2018; de Moor et al. 2019; Heap et al. 2019]. The overpressure can be alleviated by at least three mechanisms, all of which can generate explosions, potentially accompanied by collapses. (1) The overpressure exceeds the tensile strength of the surrounding rocks. Since the rocks are likely fractured and hydrothermally altered to variable extents, their strengths also may be variable and quite low in certain localities. (2) A regional earthquake can generate significant ground vibrations, causing collapses and explosions. The analysis by Montero et al. [2010] shows that such earthquakes are likely to occur along the dextral strike-slip fault system on either side of the volcano at distances of 4–22 km from the active crater. Ground shaking with peak accelerations of >0.5 g is expected for M5–M6 events along these structures. (3) A sudden strong rainfall event could also induce collapse and explosions. Our analysis shows that Feature 4 may be particularly unstable (Figures 2, 3, 6, 8). This zone appears to be highly fractured, faulted, and weakened by hydrothermal alteration, hence susceptible to external forces and events. Yet its potential to develop subsurface overpressure is unclear. We note that the linear degassing zone (Feature #2) is located 100–200 m directly east of the unstable block zone. Since active surface degassing is occurring through this linear fracture, this area may in fact have high subsurface permeability, hence a limited ability currently to pressurize.

5.4 Remote sensing platforms

An important consideration in this study was the selection of remote sensing platforms (i.e. UAV and satellite), which was guided by the spatial scale of the features being analyzed. For instance, fine-scale structural features, such as those shown in Figure 9, were examined using high-resolution UAV-derived products, whereas broader regional tectonic patterns (e.g. Figure 11) were interpreted from satellite imagery. Similarly, the phenomenon type (i.e. thermal anomaly versus 3D landscape structure) was examined based on the most appropriate data sources: thermal imagery versus photogrammetry products or satellite image basemaps.

Commercial satellite imagery can be costly. As an alternative to using actual imagery, in this study we showcased the potential for utilizing previously compiled basemaps. While these basemaps lack the spectral information of actual satellite imagery, if the user carefully considers their date of acquisition as described in the metadata (when available), some of these high spatial resolution products are sufficient for visual interpretation for larger scale landscape trends.

6 CONCLUDING REMARKS

The integrated monitoring system currently used at Poás volcano by the Observatorio Vulcanológico y Sismológico de Costa Rica (OVSICORI) may be able to detect instability prior to collapse-explosion events. Monitoring seismicity, ground deformation, thermal features, and gases is generally an effective combination. The weather station at the summit, as well as weather forecasting, could serve as an important additional tool to detect and measure significant precipitation events.

The data that we collected from the crater area by UAV has revealed a wealth of structural detail about this most active part of Poás. The combination of photogrammetric and thermal infrared information together provide new insight into the structural state of the crater, in particular the eastern sector which is unstable. Although the conditions for data collection were less than ideal at times given the highly changeable weather conditions at the summit (a common issue at active volcanic systems), we were able to obtain useful information to better understand the structural state of the crater and volcano. Rock fracturing and hydrothermal alteration, aided by sudden strong precipitation events, are likely important processes influencing instability of the crater of Poás, in particular its eastern sector. The north–south extensional fault system enhances this instability.

Hence a future combination of real-time monitoring, together with repeat surveys such as automated UAV flights on a regular basis (i.e. weekly), could enhance our ability to detect early signs of instability, prior to acceleration that could lead toward explosions and collapse events. Automated UAV flights could include LiDAR or photogrammetry, gas detectors, and thermal infrared imagers, all of which have the capability of detecting subtle changes in ground deformation, gas compositions, and thermal anomalies. Constructing this type of automated system could further allow early detection (e.g. months to possibly years) of larger magmatic and phreatomagmatic unrest and eruptions, as exemplified by the 2017 and 2025 activity.

AUTHOR CONTRIBUTIONS

Conceptualization: JS. Formal Analysis: MU, MK, J-P A-M, OL. Investigation: JS, MU, CC. Methodology: JS, MU, MK, CC. Validation: MK, MdM. Visualization: JS, MK, J-P A-M, OL. Writing original draft: JS. Writing review and editing: MK, J-P A-M, OL, MdM.

ACKNOWLEDGEMENTS

We thank Jamie Kirkpatrick for useful discussions regarding structural geology and tectonics of Costa Rica and George Leblanc for identification of the rock samples. We also thank the Sistema Nacional de Areas de Conservación (SINAC) and Administration of the Poás Volcano National Park for access to the crater. JS acknowledges ongoing financial support from the Natural Sciences and Engineering Research Council of Canada in the form of a Discovery Grant (RGPIN-2020-04197) that helped support this work. JS and MK also acknowledge support from Alliance Grant ALLRP 586350-23 from the Natural Sciences and Engineering Research Council of Canada that supported data analysis and preparation of this paper. We are grateful to two anonymous reviewers for their helpful comments which improved the paper. We also thank the editor Shreya Kanakiya for their assistance with the paper.

DATA AVAILABILITY

All data are available in the paper.

COPYRIGHT NOTICE

REFERENCES

Brown, G., H. Rymer, and R. Thorpe (1987). "The evolution of andesite volcano structures: new evidence from gravity studies in Costa Rica". *Earth and Planetary Science Letters* 82(3–4), pages 323–334. DOI: 10.1016/0012-821x(87)90206-8.

Cashman, K. V., R. S. J. Sparks, and J. D. Blundy (2017). "Vertically extensive and unstable magmatic systems: A unified view of igneous processes". *Science* 355(6331). DOI: 10.1126/science.aag3055.

D'Arcy, F., J. M. de Moor, J. Stix, A. Alan, R. Bogue, E. Corrales, J. A. Diaz, E. Mick, J. Salas-Navarro, and R. Lauzeral (2022). "New insights into carbon isotope systematics at Poás volcano, Costa Rica". *Journal of Volcanology and Geothermal Research* 431, page 107639. DOI: 10.1016/j.jvolgeores.2022.107639.

DeMets, C. (2001). "A new estimate for present-day Cocos-Caribbean Plate motion: Implications for slip along the Central American Volcanic Arc". *Geophysical Research Letters* 28(21), pages 4043–4046. DOI: 10.1029/2001gl013518.

De Moor, J. M., J. Stix, G. Avard, C. Muller, E. Corrales, J. A. Diaz, A. Alan, J. Brenes, J. Pacheco, A. Aiuppa, and T. P. Fischer (2019). "Insights on hydrothermal-magmatic interactions and eruptive processes at Poás Volcano (Costa Rica) from high-frequency gas monitoring and drone measurements". *Geophysical Research Letters* 46(3), pages 1293–1302. DOI: 10.1029/2018gl080301.

De Moor, J., A. Aiuppa, J. Pacheco, G. Avard, C. Kern, M. Liuzzo, M. Martínez, G. Giudice, and T. Fischer (2016). "Short-period volcanic gas precursors to phreatic eruptions: Insights from Poás Volcano, Costa Rica". *Earth and Planetary Science Letters* 442, pages 218–227. DOI: 10.1016/j.epsl.2016.02.056.

Drummond, K. J., G. W. Moore, X. Golovchenko, R. L. Larson, W. Pitman III, W. A. Rinehart, T. Simkin, and L. Siebert

(1986). *Plate tectonic map of the Circum-Pacific region, northeast quadrant*. Tulsa, Oklahoma: American Association of Petroleum Geologists.

Global Volcanism Program (2024). "Report on Poas (Costa Rica)". *Weekly volcanic activity report, 27 March – 2 April 2024*. Edited by S. Sennert. Weekly volcanic activity report.

– (2025). "Report on Poas (Costa Rica)". *Weekly volcanic activity report, 30 April – 6 May 2025*. Edited by S. Sennert. Weekly volcanic activity report.

Heap, M. J., V. R. Troll, A. R. L. Kushnir, H. A. Gilg, A. S. D. Collinson, F. M. Deegan, H. Darmawan, N. Seraphine, J. Neuberg, and T. R. Walter (2019). "Hydrothermal alteration of andesitic lava domes can lead to explosive volcanic behaviour". *Nature Communications* 10(1). DOI: `10.1038/s41467-019-13102-8`.

Kalacska, M., J. P. Arroyo-Mora, O. Lucanus, J. Stix, M. de Moor, C. A. Campos Vargas, and M. Urquhart (2022). "RPAS based 3D reconstruction of the eastern sector of the Poas volcano crater, Costa Rica". *Borealis* 1. DOI: `10.5683/SP3/BRJ6XU`. [Dataset].

Kuenzer, C. and S. Dech (2013). "Theoretical Background of Thermal Infrared Remote Sensing". *Thermal Infrared Remote Sensing*. Springer Netherlands, pages 1–26. ISBN: 9789400766396. DOI: `10.1007/978-94-007-6639-6_1`.

Leblanc, G., M. Kalacska, J. P. Arroyo-Mora, O. Lucanus, and A. Todd (2021). "A practical validation of uncooled thermal imagers for small RPAS". *Drones* 5(4), page 132. DOI: `10.3390/drones5040132`.

Mineo, S. and G. Pappalardo (2021). "Rock emissivity measurement for infrared thermography engineering geological applications". *Applied Sciences* 11(9), page 3773. DOI: `10.3390/app11093773`.

Montero, W., G. J. Soto, G. E. Alvarado, and W. Rojas (2010). "División del deslizamiento tectónico y transtensión en el macizo del volcán Poás (Costa Rica), basado en estudios neotectónicos y de sismicidad histórica". *Revista Geológica de América Central* (43). DOI: `10.15517/rgac.v0i43.3456`.

Mora Amador, R. A., D. Rouwet, G. González, P. Vargas, and C. Ramírez (2019). "Volcanic Hazard Assessment of Poás (Costa Rica) Based on the 1834, 1910, 1953–1955 and 2017 Historical Eruptions". *Poás Volcano*. Springer International Publishing, pages 261–299. ISBN: 9783319021560. DOI: `10.1007/978-3-319-02156-0_11`.

Observatorio Vulcanológico y Sismológico de Costa Rica (OVSICORI) (2022). "Comunicado del OVSICORI-UNA del 7 de abril 2022 sobre la erupción del volcán Poás del 6 de abril 2022". *OVSICORI internal report*.

Öhman, C. (2014). "Measurement in Thermography". *FLIR systems and the infrared training center*. Edited by C. Buchgeister, R. Danjoux, and H. Hallin. Wilsonville, Oregon: FLIR Systems.

Oppenheimer, C. and D. Stevenson (1989). "Liquid sulphur lakes at Poás volcano". *Nature* 342(6251), pages 790–793. DOI: `10.1038/342790a0`.

Pallister, J. and S. R. McNutt (2015). "Synthesis of Volcano Monitoring". *The Encyclopedia of Volcanoes*. Elsevier, pages 1151–1171. ISBN: 9780123859389. DOI: `10.1016/b978-0-12-385938-9.00066-3`.

Prosser, J. T. and M. J. Carr (1987). "Poás volcano, Costa Rica: Geology of the summit region and spatial and temporal variations among the most recent lavas". *Journal of Volcanology and Geothermal Research* 33(1–3), pages 131–146. DOI: `10.1016/0377-0273(87)90057-6`.

Robinson, P. J. and J. A. Davies (1972). "Laboratory determinations of water surface emissivity". *Journal of Applied Meteorology* 11(8), pages 1391–1393. DOI: `10.1175/1520-0450(1972)011<1391:ldowse>2.0.co;2`.

Rouwet, D., R. A. Mora Amador, L. Sandri, C. Ramírez-Umaña, G. González, G. Pecoraino, and B. Capaccioni (2019). "39 Years of Geochemical Monitoring of Laguna Caliente Crater Lake, Poás: Patterns from the Past as Keys for the Future". *Poás Volcano*. Springer International Publishing, pages 213–233. ISBN: 9783319021560. DOI: `10.1007/978-3-319-02156-0_9`.

Rowe, G. L., S. L. Brantley, M. Fernandez, J. F. Fernandez, A. Borgia, and J. Barquero (1992). "Fluid-volcano interaction in an active stratovolcano: the crater lake system of Poás volcano, Costa Rica". *Journal of Volcanology and Geothermal Research* 49(1–2), pages 23–51. DOI: `10.1016/0377-0273(92)90003-v`.

Salvage, R. O., G. Avard, J. M. de Moor, J. F. Pacheco, J. Brenes Marin, M. Cascante, C. Muller, and M. Martinez Cruz (2018). "Renewed explosive phreatomagmatic activity at Poás Volcano, Costa Rica in April 2017". *Frontiers in Earth Science* 6. DOI: `10.3389/feart.2018.00160`.

Sibaja-Brenes, J. P., A. Terada, R. A. Solís, M. C. Luna, D. U. Castro, D. P. Ramírez, R. S. Gutiérrez, M. M. Arroyo, I. Godfrey, and M. M. Cruz (2023). "Drone monitoring of volcanic lakes in Costa Rica: a new approach". *Drone Systems and Applications* 11, pages 1–14. DOI: `10.1139/dsa-2022-0023`.

Stix, J. and J. M. de Moor (2018). "Understanding and forecasting phreatic eruptions driven by magmatic degassing". *Earth, Planets and Space* 70(1). DOI: `10.1186/s40623-018-0855-z`.

Vannucchi, P. and J. P. Morgan (2019). "Overview of the Tectonics and Geodynamics of Costa Rica". *Poás Volcano*. Springer International Publishing, pages 1–12. ISBN: 9783319021560. DOI: `10.1007/978-3-319-02156-0_1`.

Vaselli, O., F. Tassi, A. Minissale, G. Montegrossi, E. Duarte, E. Fernández, and F. Bergamaschi (2003). "Fumarole migration and fluid geochemistry at Poás Volcano (Costa Rica) from 1998 to 2001". *Geological Society, London, Special Publications* 213(1), pages 247–262. DOI: `10.1144/gsl.sp.2003.213.01.15`.

Vollmer, M. and K.-P. Möllmann (2010). *Infrared Thermal Imaging: Fundamentals, Research and Applications*. Wiley. ISBN: 9783527630868. DOI: `10.1002/9783527630868`.